Nuclear Instruments and Methods in Physics Research B 581 (2026) 166344

Contents lists available at ScienceDirect

Nuclear Inst. and Methods in Physics Research, B

journal homepage: www.elsevier.com/locate/nimb

Full length article

On the stopping of Sn^{1+} ions in molecular hydrogen gas

L. Assink [a,b], T. Nieboer [a,b], J. Bijma [a], B. Neijzen [a], K. Bijlsma [a,b], L. Poirier [b,c], E. de Wit [a,b], D.J. Engels [b,c], J. Sheil [b,c], O.O. Versolato [b,c], R. Hoekstra [a,b,*]

[a] Zernike Institute for Advanced Materials, University of Groningen, Nijenborgh 3, 9747 AG, Groningen, The Netherlands
[b] Advanced Research Center for Nanolithography (ARCNL), Science Park 106, 1098 XG, Amsterdam, The Netherlands
[c] Department of Physics and Astronomy, and LaserLaB, Vrije Universiteit, De Boelelaan 1100, 1081 HV, Amsterdam, The Netherlands

ARTICLE INFO

Keywords:
Stopping cross section
Laser produced tin plasma
Retarding field analyzer

ABSTRACT

We investigate the stopping of energetic (0.13–3 keV) Sn^{1+} ions in molecular hydrogen gas using a combined experimental and modeling approach. Data on $Sn^{q+}-H_2$ collisions in this energy range is sparse, limiting a complete atomistic understanding. Time-of-flight measurements employing retarding field analyzers are used to quantify pressure-dependent shifts in flight time of Sn^{1+} ions traversing H_2 at pressures between 2×10^{-4} and 2×10^{-2} mbar. From these shifts, stopping cross sections are extracted as a function of ion energy. To interpret the measurements, a semi-classical collision model is developed, which incorporates interaction potentials derived from density functional theory and explicitly accounts for the molecular structure of H_2. The modeled stopping cross sections are in good agreement with the experimental results. Compared with other work, our dataset falls within the range reported in the literature and occupies a central position within this range.

1. Introduction

In advanced semiconductor manufacturing, extreme ultraviolet (EUV) light at a wavelength of 13.5 nm is used to pattern at the nanometer scale [1,2]. This radiation is generated by a laser-produced plasma (LPP), which is created by pulsed-laser irradiation of liquid tin droplets [3]. The emitted EUV radiation arises from transition arrays originating from singly [4–6], and even more so from multiply [7] excited configurations of several high charge states of Sn.

In addition to EUV radiation, the LPP emits a broad distribution of energetic Sn ions. Charge- and energy-resolved measurements have shown that these ions can reach kinetic energies in the keV range and that a significant fraction leaves the plasma in moderately high charge states (4 – 8+ [8]). Upon interaction with plasma-facing components, such ions can deposit a substantial amount of energy into those components and thereby reduce their lifetimes. To prevent this, EUV sources are typically operated with a hydrogen buffer gas flow. The H_2 gas slows down and mitigates expelled Sn ions without appreciably absorbing EUV radiation [9–12].

As the Sn ions propagate through the hydrogen gas, they undergo collisional processes that lead to charge-state lowering and energy loss. Traditionally, this successive charge state reduction has been assumed to stop at 2+, since the one-electron capture reaction that would produce Sn^{1+} in $Sn^{2+}+H_2$ collisions is endothermic by 1.3 eV. However, recent measurements revealed a substantial number of keV Sn^{1+} ions when the H_2 pressure was increased from base pressure to 6×10^{-4} mbar, while no substantial energy loss was yet observed [13]. It was shown by crossed-beam experiments and calculations [14] that these Sn^{1+} can originate from electron capture by metastable $Sn(^{2+}(5s5p^3P)$ ions, which are the main product ions in one-electron capture by Sn^{3+} colliding with H_2 [13]. Very recently, a second pathway was uncovered at energies below 5 keV, namely double electron capture in collisions of $Sn^{3+}+H_2$ [15], which directly leads to the production of Sn^{1+} ions. Therefore, we explicitly focus on the stopping cross sections, S, of Sn^{1+} ions in H_2 at energies of 0–3 keV rather than those of Sn^{2+}, which was previously thought to be the dominant end product of charge exchange. The stopping cross sections relate to the macroscopic stopping power, i.e., the energy loss per unit length (dE/dx) via

$$\frac{dE}{dx} = -nS, \tag{1}$$

with n the density of the target. Here, S refers to nuclear stopping. Electronic stopping contributes to less than 10% of the total stopping over the investigated energy range, as estimated using SRIM, and is therefore neglected in the present analysis. Accordingly, throughout this work, the term “stopping power” refers to nuclear stopping power.

Experimental stopping data for tin ions in molecular hydrogen gas are scarce. The only available measurements for keV Sn^{1+} and Sn^{2+} ions are reported by Abramenko et al. [16]. The commonly used

* Corresponding author.
E-mail address: r.a.hoekstra@rug.nl (R. Hoekstra).

https://doi.org/10.1016/j.nimb.2026.166344
Received 7 June 2026; Received in revised form 6 October 2026; Accepted 7 October 2026
Available online 14 October 2026
0168-583X/© 2026 The Authors. Published by Elsevier B.V. This is an open access article under the CC BY license (http://creativecommons.org/licenses/by/4.0/).

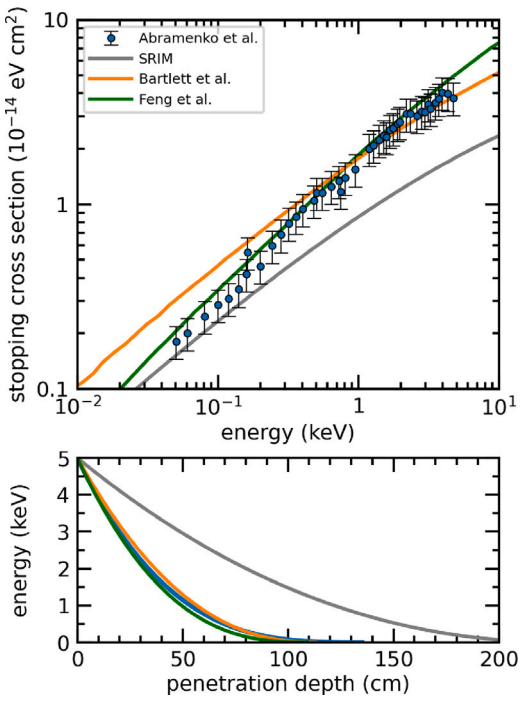


Fig. 1. Stopping cross sections for $Sn^{1+} - H_2$ data available in literature (top panel). The symbols show the experimental data, and the corresponding fit by Abramenko et al. [16] for Sn^{1+}. The orange line is the calculated stopping cross sections of Bartlett et al. [17] using slightly different interaction potentials specified by the effective nuclear charge of the target of $Z_2 = 2.76$. The green line is the calculated stopping cross section of Feng et al. [18] using a Morse potential. The gray curve show the SRIM nuclear stopping results. Using Eq. (1), the bottom panel shows the penetration depths of 5 keV Sn particles through 1 mbar of H_2 for the stopping cross section sets presented in the top panel.

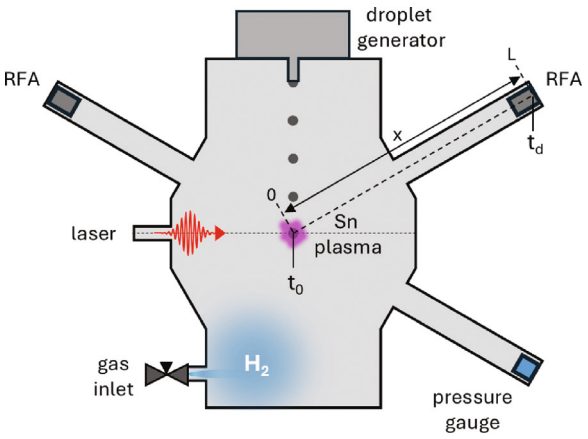


Fig. 2. Schematic of the LPP experiment used to measure time-of-flight ion spectra as a function of the hydrogen buffer gas pressure. After their creation at t_0, ions propagate over a flight distance L from the plasma source to retarding field analyzer (RFA) detectors. A total of eight RFAs are employed at two different distances from the source. The flight time of the ions is denoted by t_d.

stopping code SRIM [19,20] predicts significantly lower stopping cross sections, see Fig. 1. The sheer fact that SRIM calculates H_2 stopping cross sections that are too small was already clear from the pioneering research on the possibilities of Sn ion mitigation by gases such as H_2, He, and Ar [9,10]. The underprediction of H_2 stopping cross sections by SRIM is likely linked to its treatment of the projectile ions as neutral particles, it describes the target H_2 molecules as two H atoms, and its use of the generic ZBL (Ziegler-Biersack-Littmark) potential [19,20] as the interaction potential. Differences in the cross sections presented in literature translate directly into large uncertainties in predictions of how far Sn ions expelled from the EUV source plasma penetrate into the surrounding H_2 stopping gas, as illustrated in Fig. 1.

Bartlett et al. [17] advanced the stopping description by using density functional theory (DFT) to obtain an interatomic potential specific to the $Sn^{1+} - H_2$ system. This approach significantly improved the agreement between experiment and theory.

In this work, we present an extensive set of stopping measurements for 0.12 to 3 keV Sn^{1+} ions in H_2 gas. The energy range encompasses the transition regime in which, based on the data of Abramenko et al. [16], the stopping cross section switches from being in line with the "$Z_2 = 1$" prediction (i.e. SRIM) to the "$Z_2 = 2.76$" prediction by Bartlett et al. [17], where Z_2 is the nuclear charge of the target (more details are given in Section 2.3). The Sn ions are produced by a laser-produced plasma source installed at ARCNL in Amsterdam. The flight time of the ions from the LPP plasma to the detector is measured as a function of H_2 pressure. From the changes in ToF times, stopping cross sections are extracted. The results are compared to the existing experimental data of Abramenko et al. [16], to the simulation predictions by Bartlett et al. [17] and by Feng et al. [18], and to our own model, which extends the approach of Bartlett et al. by explicitly incorporating the two-center geometry of the H_2 molecules in energy-loss trajectory calculations.

2. Research methodology

2.1. The laser-produced plasma setup

The laser-Sn plasma EUV source installed at ARCNL, Amsterdam, used here has been described in detail in earlier work, e.g., Refs. [3,8]. A schematic overview of the parts of the ARCNL-LPP setup most relevant to this work is shown in Fig. 2.

A tin reservoir, held at a temperature of 260 °C to ensure a stable supply of molten Sn, is mounted on top of the central LPP vacuum chamber with a base pressure of approximately 1×10^{-7} mbar. Tin microdroplets are generated through an orifice in the reservoir, forming a continuous stream of droplets with a repetition rate of 22 kHz. The droplets, with a diameter of approximately 38 µm, travel downward along the vertical axis of the chamber.

Before reaching the laser-droplet interaction region, the droplet stream passes through a horizontally oriented laser light sheet. Light scattered by the droplets is detected by a photomultiplier tube, and the resulting signal is electronically down-converted to 10 Hz. This processed signal is used to trigger the Nd:YAG laser used for Sn plasma generation.

The Nd:YAG laser (at a wavelength of 1064 nm) delivers light pulses with a full-width at half-maximum (FWHM) duration of approximately 10 ns. The laser beam is focused onto the droplet to a Gaussian spot with a diameter of approximately 100 µm (FWHM). The pulse energy is adjusted using a combination of a half-wave plate and a thin-film polarizer, allowing control of the laser energy without significantly altering the beam profile. For all measurements reported here, the pulse energy was set to 90 mJ.

Ion emission from laser-produced tin plasmas is anisotropic [21]. Backward ion emission (ions coming from the back side of the target) is typically characterized by lower energies and charge states than forward emission. Consequently, low-energy 1+ ions are difficult to resolve in the forward direction, while high-energy ions are relatively scarce in the backward direction. To cover a wide range of energies, we used all our available retarding field analyzers (RFAs, of type Kimball

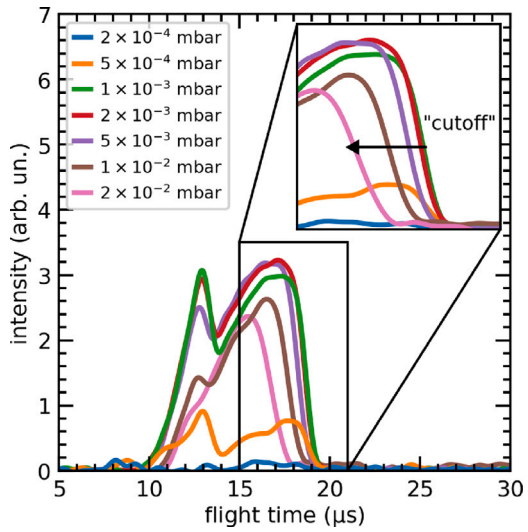


Fig. 3. Time-of-flight current traces recorded with RFA1 (see Table 1) at a retarding voltage of $V_R = 800\,V$ for hydrogen pressures between 2×10^{-4} to 2×10^{-2} mbar. The inset highlights the characteristic cutoff associated with the high-pass energy filtering at $E_d = 800\,eV$.

Physics FC-73A), positioned at various observation angles relative to the incident laser.

Two RFAs were positioned in the backward direction at a flight distance of 0.68 m from the plasma source to optimize detection of low-energy ions. The remaining six RFAs were positioned at a distance of 0.93 m. The angular positions and solid angles of all RFAs are summarized in Appendix.

Within each RFA, ions are collected by a Faraday cup biased at $V_{FC} = -30\,V$. A suppressor grid held at $V_S = -100\,V$ is used to prevent secondary electrons from entering or escaping the cup. The retarding grid voltage V_R is stepped between 0 to 4 kV in 90 increments, corresponding to a voltage step of 44.5 V. The ion current is converted to a voltage signal using a transimpedance amplifier with a gain of $25\,kV\,A^{-1}$ and a bandwidth of 25 MHz.

All measurements were performed at controlled hydrogen pressures in the range of 2×10^{-4} to 2×10^{-2} mbar. For the analysis, the gas pressure is assumed to be uniform throughout the experimental chamber. This assumption is supported by MOLFLOW+ Monte Carlo simulations reported previously [13], which showed that pressure variations along the ion trajectories (flight distance of 0.68 m) are below 5% under the present operating conditions.

2.2. Data collection and analysis

Traditional stopping experiments employ monoenergetic ion beams that pass through a gas-filled drift chamber, where the stopping cross section is either directly determined from the measured energy loss [22,23] or indirectly measured via time-of-flight (ToF) [24,25]. However, ions emitted from an LPP source exhibit a broad energy distribution. To address this, we follow the method proposed by Abramenko et al. [16] to extract stopping cross sections from such distributions by combining energy selection with time-of-flight measurements. In our approach, energy selection is achieved using the high-pass filtering characteristic of an RFA, while the laser pulse that ignites the plasma provides the ToF start signal.

The voltage V_R applied to the retarding grids of the RFA creates an electrostatic potential barrier that blocks ions with kinetic energy below $E = qV_R$, where q is the charge state of the ion. As a result, a distinct cutoff appears in the ToF spectrum at flight times corresponding to ions with kinetic energy equal to qV_R.

As an example, Fig. 3 displays ToF current traces recorded at $V_R = 800\,V$ for a set of H_2 pressures covering a pressure range of 2×10^{-4} to 2×10^{-2} mbar. With increasing hydrogen pressure, changes are observed in the spectral shape, amplitude, and cutoff position. At the lowest pressures, the signal increases with pressure, while the cutoff position remains unchanged within the experimental uncertainty. At higher pressures, a shift of the cutoff towards shorter flight times emerges. At the same time, the spectral shape near the cutoff changes, and the detected ion current decreases.

These observations are in full agreement with the findings of Rai et al. [13]. They showed that, at low pressures of the LPP surrounding H_2 gas, electron capture by Sn^{q+} ions ($q > 1+$) rapidly reduces the charge states to 1+, thereby increasing the fraction of Sn^{1+} ions. This charge-state lowering precedes appreciable collisional energy loss. Only at higher pressures does energy loss become significant, leading to measurable cutoff shifts and a reduction in signal. Charge-state lowering and energy loss can thus be considered not to interweave with one another.

At sufficiently high H_2 pressures in the energy loss regime, the ion energy at position x along its trajectory from plasma to detector is defined by $E(x) = E_0 - \Delta E(x)$, where E_0 is the initial energy of the ion upon being expelled from the plasma, and $\Delta E(x)$ represents the integral energy loss between 0 and x. When a Sn ion of mass M loses energy, its velocity decreases. Consequently, one has to integrate over its actual velocity $v(x)$ to determine the ToF T from plasma to the detector positioned at a distance L:

$$T = \int_0^L \frac{dx}{v(x)} = \int_0^L \sqrt{\frac{M}{2E(x)}}\,dx. \tag{2}$$

The straight-line trajectory assumed in the above derivation is well justified for the present system. The maximum scattering angle for an elastic Sn – H_2 collision is just below 1°, corresponding to an impact parameter of 0. Most collisions occur at larger impact parameters and therefore result in substantially smaller deflections. As an example, for the 1×10^{-2} mbar case shown in Fig. 3, the observed cutoff shift corresponds to an energy loss of approximately 150 eV (from 950 to 800 eV). At these ion energies, the binary collision approximation gives an energy loss of approximately 30 eV for maximum-angle scattering. Even if the total energy loss were a consequence of five consecutive maximum-angle collisions, the 0.68 m flight path would increase by only 0.4%. Thus, the effect of scattering on the flight distance can be neglected.

In the experiment, the initial energy of the ions is unknown. Ions are filtered on their energy E_d upon arrival at the detector. Therefore, it is more convenient to express $E(x)$ as $E_d + \Delta E'(x)$, where $\Delta E'(x)$ is the energy that the ion still has to lose between x and the position of the detector, L. With this substitution, Eq. (2) can be rewritten as:

$$T = \sqrt{\frac{M}{2E_d}} \int_0^L \frac{dx}{\sqrt{1 + \frac{\Delta E'(x)}{E_d}}}. \tag{3}$$

If there is no H_2 gas, there is no energy loss and $T = T_{vac} = L\sqrt{M/(2E_d)}$. For $\Delta E'(x)$ much smaller than E_d, a first-order Taylor expansion of the denominator can be applied, yielding:

$$T \backsimeq T_{vac}\left(1 - \frac{1}{2E_d L}\int_0^L \Delta E'(x)\,dx\right). \tag{4}$$

The ToF difference $\Delta T = T - T_{vac}$ is the experimental observable that can be linked to the stopping cross sections. From Eq. (4), it follows that:

$$\Delta T = -\frac{T_{vac}}{2E_d L}\int_0^L \Delta E'(x)\,dx. \tag{5}$$

Using Eq. (1), $\Delta E'(x)$ can be written as:

$$\Delta E'(x) = \int_x^L nS\,dx \backsimeq nS(L - x), \tag{6}$$

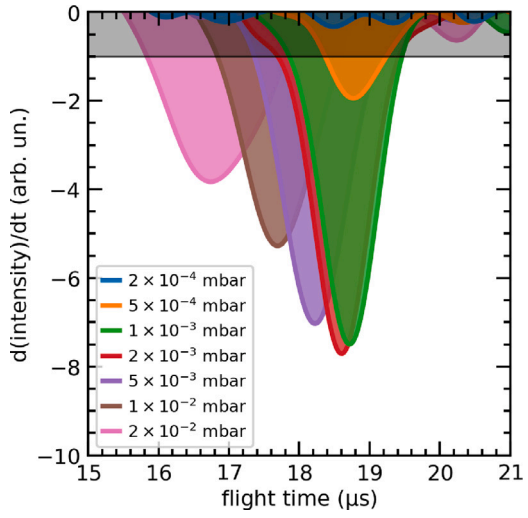


Fig. 4. Derivatives of ToF traces taken at a retarding voltage of $V_R = 800$ V for H_2 pressures in the range of 2×10^{-4} to 2×10^{-2} mbar (same dataset as in Fig. 3). The positions of the minima mark the ions' ToF at the cutoff. The dashed line indicates the threshold acceptance level applied in the analysis; the dark shaded region above the line denotes values below this threshold.

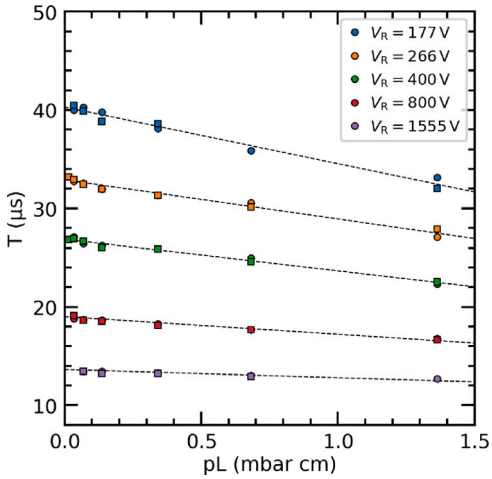


Fig. 5. Peak positions of the differentiated current traces associated with the Sn^{1+} cutoffs as a function of the hydrogen pressure-length product pL for the two RFAs located at a flight distance of 0.68 m (RFA1 & RFA2, see Table 1). The dashed lines represent the linear fits to the data, from which the stopping cross sections are extracted.

where, in the second step, it is assumed that S is constant over the full path length, which is justified if the total energy loss from the source to the detector is small compared to the ion's kinetic energy.

If we substitute Eq. (6) for the residual energy loss into the equation for the time-of-flight shift ΔT (Eq. (5)), we find:

$$\Delta T = -\frac{T_{\mathrm{vac}} n S}{2 E_{\mathrm{d}} L} \int_0^L (L - x)\, dx = -\frac{T_{\mathrm{vac}} n S L}{4 E_{\mathrm{d}}}. \tag{7}$$

Thus, the stopping cross section as a function of kinetic energy can be extracted via

$$S(E) = -\frac{4E}{T_{\mathrm{vac}}} \frac{\Delta T}{nL}. \tag{8}$$

The key experimental parameter is ΔT, which relies on a consistent determination of flight times with and without H_2 gas present. For determination of the ions' ToF, the long-flight-time cutoff edges of the ToF traces (see Fig. 3) are used, specifically their inclination points. These inclination points are identified by taking the derivative of the ToF traces, resulting in Gaussian-like peaks centered at the flight times marking the inclination point of the falling ToF edge. For the same set of H_2 pressures as shown in Fig. 3, Fig. 4 presents the derivatives of the ToF traces. The peak positions, which define the ion cutoff flight times T, decrease smoothly with H_2 pressure, from 18.7 μs at 5×10^{-4} mbar to 16.5 μs at 2×10^{-2} mbar. To exclude artificial dips arising from noise or signal fluctuations, a threshold level of approximately 10% of the strongest dip is applied.

For five RFA barrier voltage settings, Fig. 5 shows the extracted peak positions as a function of the H_2 column density nL (represented here by the product of pressure and distance, pL). The underlying ToF traces were recorded with the two RFAs located at a distance of 0.68 m from the LPP. The slopes of linear fits to these data yield the ratio $\Delta T/nL$, which is required to calculate the stopping cross section (cf. Eq. (8)). The fits are performed with the intercept on the ToF axis fixed at T_{vac}. The same procedure was applied to the datasets obtained with the RFAs positioned at 0.93 m.

The resulting stopping cross sections are presented in Fig. 6. The datasets obtained at the two flight distances show very good agreement in the overlapping energy range between approximately 0.3 and 2 keV. The shorter flight distance allows extraction of stopping data at lower energies, while the longer distance provides improved sensitivity at higher energies. Together, the two configurations enable the determination of the stopping cross section over the full investigated energy range. The agreement between results obtained at two different flight distances (0.68 m and 0.93 m) demonstrates the consistency of the method and confirms that the derived stopping cross sections are not sensitive to the specific detector geometry or the underlying ion energy distribution within the present uncertainties. Therefore, in the final comparison to other data (see Section 3), the average of the two datasets is used.

The dominant systematic uncertainty in the extracted stopping cross section is expected to originate from the accuracy of the H_2 pressure, as the stopping cross section is directly determined from the pressure-dependent ToF shift. A small systematic offset in the absolute pressure would result in a corresponding shift of the extracted stopping cross section, either slightly upwards or downwards, while leaving the relative trends largely unaffected. The good agreement between measurements performed with flight-tube lengths of 0.68 m and 0.93 m provides an independent consistency check on the measurements and analysis procedure, indicating that geometry-dependent systematic effects are small within the experimental uncertainty.

For further discussion in Section 3, two power-law trend lines of the form $S \propto E^{\alpha}$ are included, with $\alpha = 1$ and $\alpha = 0.35$, representing the approximate low- and high-energy dependencies of the data, respectively.

2.3. Modeling of the stopping cross sections

The universal stopping code SRIM [19,20] underestimates the experimental stopping cross sections (see Fig. 1). The three main reasons for this discrepancy are likely: (i) projectile ions are treated as neutral particles, (ii) the target H_2 molecule is approximated as two independent hydrogen atoms, and (iii) the use of the generic ZBL potential [19, 20].

Bartlett et al. [17] addressed this limitation by calculating the potential energy surface (PES) specific to the three-center nature of the Sn^{1+} – H_2 system, thereby explicitly taking the charge state of the Sn ion into account. In their approach, the PES was calculated using density functional theory (DFT) with the NWCHEM package [26]. A central ZBL potential was subsequently fitted to the radial average of

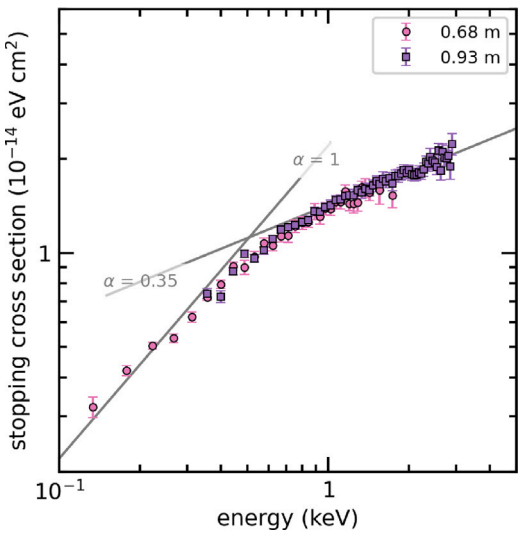


Fig. 6. Experimental stopping cross sections derived from time-of-flight measurements at hydrogen pressures in the range of 2×10^{-4} to 2×10^{-2} mbar. The figure shows results obtained from the two RFAs located at 0.68 m (pink dots) and from the six RFAs at 0.93 m (purple squares). The two datasets exhibit strong agreement in the overlapping energy region between approximately 0.3 and 2 keV. The solid gray lines represent power-law fits of the form $S \propto E^{\alpha}$, with the corresponding exponent α indicated next to each trend line.

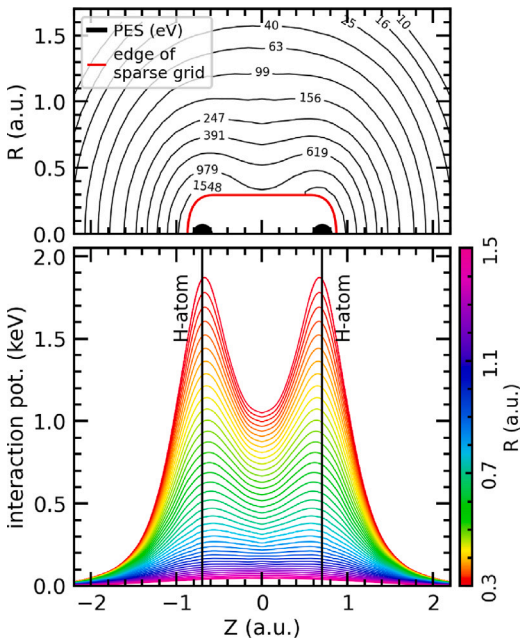


Fig. 7. Potential energy surface (PES) of the Sn^{1+} – H_2 system used in the GIonS model. The top panel shows a contour plot of the PES (in eV) in the molecular plane, with the positions of the hydrogen atom indicated by the black circles. The red curve denotes the boundary between the C-grid and R-grid sparse sampling regions. The bottom panel shows one-dimensional line-outs of the PES as a function of the projectile coordinate Z for different perpendicular distances R, as indicated by the color scale. The vertical lines mark the positions of the hydrogen atoms.

the DFT interaction potential by tuning the effective target charge Z_2, for which a value of 2.76 was found to be optimal. Implementing this modified ZBL potential in conventional stopping codes such as SRIM resulted in stopping cross sections that are in good agreement with the experimental data of Abramenko et. al. [16].

Alongside the reported measurements, an in-house quasi-classical collision model, referred to as GIonS (Groningen Ion Stopping), was developed. In contrast to the effective central-potential approach of Bartlett et al. [17], GIonS retains the full non-central, molecular character of the interaction potential in the energy-loss calculations. The interaction potential is obtained from DFT calculations using the NWCHEM package, employing the range-separated hybrid functional rCAM-B3LYP [27]. Relativistic effects for the heavy Sn atom are accounted for through the basis set and effective core potential rather than through the rCAM-B3LYP functional itself. The def2-TZVPPD basis-set of the Ahlrichs def2-XZVP basis-set family [28,29] was used, in combination with the ECP28MDF effective core potential [30]. Rather than constructing the potential on a uniform grid, the PES is sampled on two complementary sparse grids, referred to as the R- and C-grid. The C-grid covers a half-sphere centered on each hydrogen nucleus, spanning radial distances from 5 a.u. down to 0.3 a.u., and captures interactions in the vicinity of each nucleus. In contrast, the R-grid is a rectangular grid extending 5 a.u. perpendicular to the molecular axis and 1.7 a.u. parallel to it, thereby covering the full extent of the H_2 molecule. The C-grid is constructed using Clenshaw-Curtis nodes, while the R-grid employs Chebyshev nodes, allowing for efficient sampling and reducing interpolation artifacts such as Runge's phenomenon [31,32]. The discrete DFT data points obtained on both grids are combined into a single representation of the PES and interpolated using the Tasmanian sparse grid package [33,34], yielding a continuous potential that can be evaluated at arbitrary positions in space. Contour plots and representative line-outs of the potential energy surface are shown in Fig. 7.

Energy-loss calculations are then performed for specific ion trajectories through the interpolated PES. For each trajectory, characterized by a given impact parameter (up to 40 a.u.), the interaction potential is evaluated along the ion path and integrated to obtain the energy loss. Due to the molecular nature of the target, these calculations are repeated for many orientations of the H_2 molecule, and the results are averaged accordingly. This procedure is carried out for projectile energies ranging from 0.1 to 5 keV.

Fig. 8 shows a systematic comparison of different model approximations of the molecular hydrogen structure. The lowest set of curves consists of calculations for atomic hydrogen and serves as a comparison of the different stopping codes: SRIM and GIonS. As can be seen, the results coincide, as both codes use the same ZBL Sn – H interaction potential. The other curves represent molecular hydrogen calculations with different approximations to the interaction potentials used. In GIonS-ZBL-2H, H_2 is approximated by two independent H atoms separated by the internuclear distance of the molecule, with their respective potentials added linearly. The other two curves are based on DFT calculations of the potential energy surface. For their stopping calculations, Bartlett et al. fitted a ZBL-type potential to their spherically averaged DFT PES and found that the best representation was obtained using $Z_2 = 2.76$. In GIonS-DFT, the full DFT PES is retained, thereby maintaining the non-spherical molecular structure of the H_2 target. Thus, approximating the molecular target by a spherically symmetric potential affects appreciably the calculated stopping power, highlighting the importance of retaining the actual non-spherical shape of the molecule.

3. Discussion

Fig. 9 compares our experimental and model stopping cross sections for keV Sn^{1+} ions in molecular hydrogen with all other available datasets. Similar to the experimental results of Abramenko et al. [16], our data exhibit a pronounced increase below 1 keV and a gradual leveling off above this energy. However, on an absolute scale, our

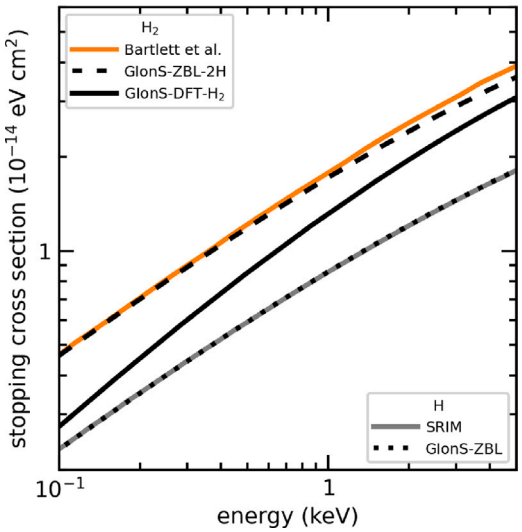


Fig. 8. Systematic comparison for different approximations of the molecular H_2 structure. The lowest set of curves shows calculations for atomic hydrogen using SRIM (gray curve) and GIonS (black dotted curve). The remaining curves show H_2 calculations using different descriptions of the molecular interaction potential: GIonS-ZBL-2H (black dashed curve), the approach by Bartlett et al. [17] (orange curve), and GIonS-DFT-H_2 (black curve).

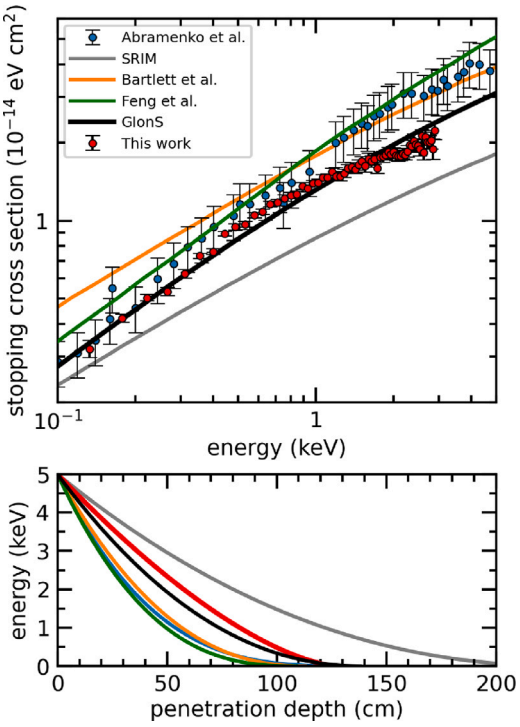


Fig. 9. Stopping cross sections for Sn^{1+} ions in H_2 as a function of impact energy (top panel). The present experimental results (red symbols) are compared to calculations from the GIonS model (black curve), as well as to literature data from Abramenko et al. [16] (blue symbols), Bartlett et al. [17] (orange curve), Feng et al. [18] (green curve), and SRIM (gray curve). The bottom panel shows the penetration depths of 5 keV Sn particles through 1 mbar of H_2 for the stopping cross section sets presented in the top panel.

measured stopping cross sections are on average about 20% lower than those reported by Abramenko et al. Slightly above 1 keV, their data appear to make a step to somewhat higher values, which enlarges the difference between the two datasets to about 50%. At the high-energy side, both datasets appear to approach a plateau.

The available model calculations do not provide a single unique description of the stopping cross section over the energy range from 0.1 to 5 keV. SRIM systematically underestimates the measured stopping cross sections across the full energy range. The modeling results of Bartlett et al. [17] show a clear improvement over SRIM. Instead of the common ZBL potential used by SRIM, Bartlett et al. used a modified ZBL potential fitted to potential energies obtained from DFT calculations. The best agreement with the DFT results was achieved by adjusting the effective nuclear charge Z_2 to 2.76. For collision energies above approximately 1 keV, this modified ZBL potential shows good agreement with the data of Abramenko et al.

More recently, Feng et al. [18] calculated potential energy surfaces for *neutral* Sn on H_2 using DFT, which they fitted with a Morse potential, which inherently includes an attractive potential-energy well. In this way, the model mimics the potential-energy well present in the ionic Sn^{1+} – H_2 system due to polarization effects. The resulting stopping cross sections based on the Morse potential exhibit a steeper increase with collision energy and do not yet level at higher energies. However, below 1 keV, they are in somewhat better agreement with the experimental data.

As described in Section 2.3, our GIonS model is likewise based on DFT-derived interaction potentials, but explicitly retains the molecular structure of H_2 in the calculation of stopping cross sections. Over the full energy range accessible in the present experiment (0.1–3 keV), the GIonS results are in very good agreement with our experimental stopping cross sections. Small deviations are observed around 0.7 keV and at the highest energies. The calculated cross sections lie between the $Z_2 = 2.76$ prediction by Bartlett et al. [17] and SRIM.

More clearly than the data of Abramenko et al. [16] and previous calculations, both our experimental and modeled results show a smooth transition in the energy dependence of the stopping cross section, from an approximately E^1 scaling to an $E^{0.35}$ scaling. This indicates that the investigated energy range encompasses the transition from one collision regime to another (see also Fig. 9).

At collision energies well below 1 keV/u, the system remains deep in the nuclear stopping regime (see, e.g., reviews [35–38]). In this low-energy limit, the stopping cross section scales linearly with collision energy, which is characteristic of hard-sphere (or billiard-ball-type) elastic collisions. This hard-sphere approximation holds for energies where the distance of closest approach is larger than the (Firsov) screening length a_F of the appropriate screened Coulomb potential. In atomic units, this length is given by $a_F = 0.8853(\sqrt{Z_1} + \sqrt{Z_2})^{-2/3}$, where Z_1 and Z_2 denote the nuclear charge state of the projectile and target atom, respectively. For the present system, $a_F \approx 0.25$ a.u.

Our measurements show a transition from hard-sphere behavior at collision energies of approximately 600 eV (cf. Fig. 6). According to the potential energy surface shown in the top panel of Fig. 7, 600 eV facilitates a distance of closest approach of about 0.5 a.u., i.e., roughly twice the screening length a_F. However, at these low energies, one might assume that the inner-shell electrons of Sn efficiently act as inert spectators (fully shielding the Sn nucleus), such that only the outer $5s^25p$ electrons contribute to the interaction. This would imply an effective nuclear charge state of $Z_1 = 4$ instead of 50, increasing a_F from approximately 0.25 to nearly 0.45 a.u., thereby bringing the two length scales into closer agreement.

At higher energies, just above the hard-sphere regime, the use of Thomas–Fermi and Moliere potentials leads to an approximate $E^{1/3}$ scaling of the stopping cross section [35,38]. This is close to the exponent of 0.35 obtained from our measurements (see Fig. 6).

4. Conclusion

In this work, we have investigated the stopping of slow (0.13–3 keV) Sn^{1+} ions in H_2 gas by combining time-of-flight measurements with energy selection using retarding field analyzers. From the analysis of the pressure-dependent shifts in the time-of-flight spectra, absolute stopping cross sections were determined over more than an order of magnitude in ion energy.

The measured stopping cross sections show excellent agreement with the results of our GIonS semi-classical collision model. Similar to the work of Bartlett et al. [17], the model is based on DFT-calculated interaction potentials. While other DFT-based approaches [17,18] fit centrosymmetric potentials to DFT potential energy surfaces, GIonS directly retains the full DFT PES in the calculation of stopping cross sections. The energy dependence of both the measured and calculated stopping cross sections agrees with available literature data in the nuclear stopping regime.

Our results confirm that the commonly used SRIM package systematically underestimates stopping cross sections for slow, heavy ions in molecular gases at low energies. At the same time, our cross sections are more than 40% lower than the only other experimental dataset by Abramenko et al. [16] at energies above 1 keV, whereas good agreement is found at the lowest energies (0.1–0.25 keV). Since the penetration depth of Sn^{1+} ions in an H_2 stopping gas exponentially depends on the stopping cross sections, an uncertainty of 20% or less is desirable for reliable predictive modeling of the stopping of Sn ions expelled from EUV lithography sources.

These discrepancies highlight the need for further experimental and theoretical work. In particular, given the broad energy distributions of ions escaping EUV source plasmas and the uncertainties in the exact composition of the gas surrounding the EUV plasma, experiments using monoenergetic Sn ion beams may provide a more controlled route towards improved accuracy.

CRediT authorship contribution statement

L. Assink: Writing – original draft, Visualization, Software, Methodology, Investigation, Formal analysis, Data curation. **T. Nieboer:** Writing – review & editing, Software, Investigation. **J. Bijma:** Software, Investigation. **B. Neijzen:** Methodology, Investigation. **K. Bijlsma:** Writing – review & editing, Investigation. **L. Poirier:** Investigation. **E. de Wit:** Writing – review & editing, Investigation. **D.J. Engels:** Writing – review & editing, Investigation. **J. Sheil:** Writing – review & editing, Supervision, Resources. **O.O. Versolato:** Writing – review & editing, Supervision, Resources. **R. Hoekstra:** Writing – original draft, Supervision, Resources, Project administration, Methodology, Funding acquisition, Conceptualization.

Declaration of competing interest

The authors declare the following financial interests/personal relationships which may be considered as potential competing interests: John Sheil reports financial support was provided by Dutch Research Council. If there are other authors, they declare that they have no known competing financial interests or personal relationships that could have appeared to influence the work reported in this paper.

Acknowledgments

This work was conducted as part of the research program of the Advanced Research Center for Nanolithography (ARCNL), a public–private partnership of the University of Amsterdam (UvA), Vrije Universiteit Amsterdam, Rijksuniversiteit Groningen (RUG), the Dutch Research Council (NWO), and the semiconductor equipment manufacturer ASML. This publication is part of ARIES Project No. 20152 of the research program VENI which is financed by NWO.

Table 1
Geometrical configuration of the retarding field analyzers used in the present experiment. The table lists the detector positions in terms of their distance from the plasma source and their angular orientation with respect to the laser propagation axis, given by the polar angle α, elevation β, and azimuth γ.

RFA	d (m)	$\alpha(^\circ)$	$\beta(^\circ)$	$\gamma(^\circ)$	$\Delta\Omega(\mu sr)$
1	0.68	139	30	150	44
2	0.68	150	30	180	44
3	0.93	30	30	0	23
4	0.93	41	−30	30	23
5	0.93	64	30	60	23
6	0.93	64	30	300	23
7	0.93	90	30	90	23
8	0.93	120	30	120	23

Appendix

In this Appendix, the geometrical configuration of the retarding field analyzers (RFAs) used in the present experiments is specified. The RFAs are positioned at different observation angles with respect to the incident laser direction to sample ions emitted over a wide angular range. A total of eight RFAs are employed. Two detectors are placed in the backward direction at a flight distance of 0.68 m from the plasma source, where low-energy ions are most prominent. The remaining six RFAs are positioned at a distance of 0.93 m and cover forward and intermediate emission angles, where higher-energy and higher charge-state ions dominate.

Each RFA is mounted on a fixed port of the vacuum chamber, defining its observation angle relative to the laser propagation axis. The detector acceptance is determined by its aperture and distance from the source, resulting in a well-defined solid angle. Table 1 summarizes the detector distances and the angular positions in terms of the angle with respect to the laser axis (α), elevation (β), and azimuth (γ).

Data availability

Data will be made available on request.

References

[1] V. Bakshi, EUV lithography, SPIE Press, 2018.
[2] I. Fomenkov, D. Brandt, A. Ershov, A. Schafgans, Y. Tao, G. Vaschenko, S. Rokitski, M. Kats, M. Vargas, M. Purvis, R. Rafac, B.L. Fontaine, S.D. Dea, A. LaForge, J. Stewart, S. Chang, M. Graham, D. Riggs, T. Taylor, M. Abraham, D. Brown, Light sources for high-volume manufacturing EUV lithography: technology, performance, and power scaling, Adv. Opt. Techn. 6 (2017) 173–186.
[3] O.O. Versolato, J. Sheil, S. Witte, W. Ubachs, R. Hoekstra, Microdroplet-tin plasma sources of EUV radiation driven by solid-state-lasers, J. Opt. 24 (2022) 054014.
[4] G. O'Sullivan, B. Li, R. D'Arcy, P. Dunne, P. Hayden, D. Kilbane, T. McCormack, H. Ohashi, F. O'Reilly, P. Sheridan, E. Sokell, C. Suzuki, T. Higashiguchi, Spectroscopy of highly charged ions and its relevance to EUV and soft X-ray source development, J. Phys. B: At. Mol. Opt. Phys. 48 (2015) 144025.
[5] S. Fujioka, H. Nishimura, K. Nishihara, A. Sasaki, A. Sunahara, T. Okuno, N. Ueda, T. Ando, Y. Tao, Y. Shimada, K. Hashimoto, M. Yamaura, K. Shigemori, M. Nakai, K. Nagai, T. Norimatsu, T. Nishikawa, N. Miyanaga, Y. Izawa, K. Mima, Opacity effect on extreme ultraviolet radiation from laser-produced tin plasmas, Phys. Rev. Lett. 95 (23) (2005) 1–4.
[6] J. Colgan, D. Kilcrease, J. Abdallah, M. Sherrill, C. Fontes, P. Hakel, G. Armstrong, Atomic structure considerations for the low-temperature opacity of Sn, High Energy Density Phys. 23 (2017) 133–137.
[7] F. Torretti, J. Sheil, R. Schupp, M.M. Basko, M. Bayraktar, R.A. Meijer, S. Witte, W. Ubachs, R. Hoekstra, O.O. Versolato, A.J. Neukirch, J. Colgan, Prominent radiative contributions from multiply-excited states in laser-produced tin plasma for nanolithography, Nat. Commun. 11 (2020) 1–8.
[8] L. Poirier, A.C. Lassise, R. Hoekstra, J. Sheil, O.O. Versolato, Laser-intensity dependence of ion emission from Nd:YAG-laser-produced plasma expanding into vacuum, Phys. Plasmas 30 (2023) 083505.
[9] S.S. Harilal, B. O'Shay, Y. Tao, M.S. Tillack, Ambient gas effects on the dynamics of laser-produced tin plume expansion, J. Appl. Phys. 99 (2006) 083303.

[10] S.S. Harilal, B. O'Shay, Y. Tao, M.S. Tillack, Ion debris mitigation from tin plasma using ambient gas, magnetic field and combined effects, Appl. Phys. B 86 (2007) 547–553.
[11] D. Bleiner, T. Lippert, Stopping power of a buffer gas for laser plasma debris mitigation, J. Appl. Phys. 106 (2009) 123301.
[12] T. Wu, X. Wang, H. Lu, P. Lu, Debris mitigation power of various buffer gases for CO_2 laser produced tin plasmas, J. Phys. D: Appl. Phys. 45 (2012) 475203.
[13] S. Rai, K.I. Bijlsma, L. Poirier, E. de Wit, L. Assink, A.C. Lassise, I. Rabadan, L. Mendez, J. Sheil, O.O. Versolato, R. Hoekstra, Evidence of production of keV Sn^+ ions in the H_2 buffer gas surrounding a Sn-plasma EUV source, Plasma Sources Sci. Technol. 32 (2023) 035006.
[14] K. Bijlsma, L. Oltra, E. de Wit, L. Assink, I. Rabadan, L. Mendez, R. Hoekstra, Electron capture from molecular hydrogen by metastable Sn^{2+*} ions, Atoms 12 (2024) 9.
[15] L. Oltra, I. Rabadán, L. Méndez, K. Bijlsma, E. de Wit, R. Hoekstra, Sequential synchronous mechanism for double-electron capture: insights into unforeseen large cross sections in low-energy Sn^{3+} + H_2 collisions, Phys. Rev. Lett. 134 (2025) 093002.
[16] D.B. Abramenko, M.V. Spirodonov, P.V. Krainov, V.M. Krivtsun, D.I. Astakhov, V.V. Medvedev, M. van Kampen, D. Smeets, K.N. Koshelev, Measurements of hydrogen gas stopping efficiency for tin ions from laser-produced plasma, Appl. Phys. Lett. 112 (2018) 164102.
[17] N. Bartlett, A. Herschberg, J. Crouse, T. Dallal, J. Nuttal, J. Stahl, N. Braaksma, D. Ruzic, Elastic scattering cross sections and transport of tin ions in extreme ultraviolet lithography sources, Phys. Scr. 99 (2024) 065411.
[18] X. Feng, Y. Song, Y. Ma, B. Li, DFT-based interatomic potentials for hydrogen-metal systems: Improved stopping power modeling, Nucl. Instrum. Methods Phys. Res. B 572 (2026) 165999.
[19] J.F. Ziegler, J.P. Biersack, M.D. Ziegler, SRIM - the Stopping and Range of Ions in Matter, Ion Implantation Press, 2008.
[20] J.F. Ziegler, M.D. Ziegler, J.P. Biersack, SRIM – The stopping and range of ions in matter (2010), Nucl. Instrum. Methods Phys. Res. B 268 (11) (2010) 1818–1823.
[21] L. Poirier, D.J. Hemminga, A.C. Lassise, L. Assink, R. Hoekstra, J. Sheil, O.O. Versolato, Strongly anisotropic ion emission in the expansion of Nd:YAG-laser-produces plasma, Phys. Plasmas 29 (2022) 123102.
[22] G. Sidenius, Systematic stopping cross-section measurements with low-energy ions in gases, Mat. Fys. Dan. Vid. Selsk 19 (1974) 1–32.
[23] P. Hvelplund, Energy loss and straggling of 100-500-keV $_{90}$Th, $_{82}$Pb, $_{80}$Hg, and $_{64}$Gd in H_2, Phys. Rev. A 11 (1975) 1921.
[24] V. Martini, Energy loss measurements of kev-ions in gases by time-of-flight spectroscopy, Nucl. Instr. Meth. 124 (1975) 119–124.
[25] K. Freitag, D. Reschke, E. Geyer, Stopping power measurements for low energy ions in gases by time-of-flight spectroscopy, Nucl. Instrum. Methods Phys. Res. B 27 (1987) 344–352.
[26] E. Aprà, E.J. Bylaska, W.A. de Jong, N. Govind, K. Kowalski, T.P. Straatsma, M. Valiev, H.J.J. van Dam, Y. Alexeev, J. Anchell, V. Anisimov, F.W. Aquino, R. Atta-Fynn, J. Autschbach, N.P. Bauman, J.C. Becca, D.E. Bernholdt, K. Bhaskaran-Nair, S. Bogatko, P. Borowski, J. Boschen, J. Brabec, A. Bruner, E. Cauët, Y. Chen, G.N. Chuev, C.J. Cramer, J. Daily, M.J.O. Deegan, T.H. Dunning Jr., M. Dupuis, K.G. Dyall, G.I. Fann, S.A. Fischer, A. Fonari, H. Früchtl, L. Gagliardi, J. Garza, N. Gawande, S. Ghosh, K. Glaesemann, A.W. Götz, J. Hammond, V. Helms, E.D. Hermes, K. Hirao, S. Hirata, M. Jacquelin, L. Jensen, B.G. Johnson, H. Jónsson, R.A. Kendall, M. Klemm, R. Kobayashi, V. Konkov, S. Krishnamoorthy, M. Krishnan, Z. Lin, R.D. Lins, R.J. Littlefield, A.J. Logsdail, K. Lopata, W. Ma, A.V. Marenich, J. Martin del Campo, D. Mejia-Rodriguez, J.E. Moore, J.M. Mullin, T. Nakajima, D.R. Nascimento, J.A. Nichols, P.J. Nichols, J. Nieplocha, A. Otero-de-la-Roza, B. Palmer, A. Panyala, T. Pirojsirikul, B. Peng, R. Peverati, J. Pittner, L. Pollack, R.M. Richard, P. Sadayappan, G.C. Schatz, W.A. Shelton, D.W. Silverstein, D.M.A. Smith, T.A. Soares, D. Song, M. Swart, H.L. Taylor, G.S. Thomas, V. Tipparaju, D.G. Truhlar, K. Tsemekhman, T. Van Voorhis, Á. Vázquez-Mayagoitia, P. Verma, O. Villa, A. Vishnu, K.D. Vogiatzis, D. Wang, J.H. Weare, M.J. Williamson, T.L. Windus, K. Woliński, A.T. Wong, Q. Wu, C. Yang, Q. Yu, M. Zacharias, Z. Zhang, Y. Zhao, R.J. Harrison, NWChem: Past, present and future, J. Chem. Phys. 152 (2020) 184102.
[27] A.J. Cohen, P. Mori-Sánchez, W. Yang, Development of exchange-correlation functionals with minimal many-electron self-interaction error, J. Chem. Phys. 126 (2007) 191109.
[28] F. Weigend, R. Ahlrichs, Balanced basis sets of split valence, triple zeta valence and quadruple zeta valence quality for H to Rn: Design and assessment of accuracy, Phys. Chem. Chem. Phys. 7 (2005) 3297–3305.
[29] D. Rappoport, F. Furche, Property-optimized Gaussian basis sets for molecular response calculations, J. Chem. Phys. 133 (2010) 134105.
[30] B. Metz, H. Stoll, M. Dolg, Small-core multiconfiguration-Dirac–Hartree–Fock-adjusted pseudopotentials for post-d main group elements: Application to PbH and PbO, J. Chem. Phys. 113 (2000) 2563–2569.
[31] J. Stoer, R. Bulirsch, Introduction to Numerical Analysis, Springer, 2002.
[32] L.N. Trefethen, Approximation Theory and Approximation Practice, SIAM, 2013.
[33] M. Stoyanov, D. Lebrun-Grandie, J. Burkardt, D. Munster, Tasmanian, 2013, Version 9. https://github.com/ORNL/Tasmanian.
[34] M. Stoyanov, User Manual: Tasmanian Sparse Grids, Tech. Rep. ORNL/TM-2015/596, Oak Ridge National Laboratory, One Bethel Valley Road, Oak Ridge, TN, 2015.
[35] K.B. Winterbon, P. Sigmund, J.B. Sanders, Spatial distribution of energy deposited atomic particles in elastic collisions, K. Dan. Vidensk. Selsk. Mat. Fys. Medd. 37 (1970) 5–73.
[36] W. Eckstein, Computer Simulation of Ion-Solid Interactions, Springer, 1991.
[37] R. Smith, Atomic and Ion Collisions in Solids and at Surfaces: Theory, Simulations and Applications, Cambridge University Press, 1997.
[38] P. Sigmund, Stopping of Heavy Ions: a Theoretical Approach, Springer, 2004.